Ray-tracing image simulations of transparent objects with complex shape and inhomogeneous refractive index

Armin Kalita,[1] Bryan Oller,[1] Thomas Paula,[2] Alexander Bußmann,[2] Sebastian Marte,[1] Gabriel Blaj,[3]
Raymond G. Sierra,[4] Sandra Mous,[4] Kirk A. Larsen,[4] Xinxin Cheng,[4] Matt J. Hayes,[4]
Kelsey Banta,[4] Stella Lisova,[4] Peter Nguyen,[4] Serge A. H. Guillet,[4] Divya Thanasekaran,[4]
Silke Nelson,[4] Mengning Liang,[4] Stefan Adami,[2] Nikolaus A. Adams,[2] and Claudiu A. Stan[1, *]

[1]*Department of Physics, Rutgers University-Newark, Newark, NJ 07102, USA*
[2]*Chair of Aerodynamics and Fluid Mechanics, TUM School of Engineering and Design,*
Technical University of Munich, 85748 Garching bei München, Germany
[3]*Technology Innovation Directorate, SLAC National Accelerator Laboratory, Menlo Park, CA 94025, USA*
[4]*Linac Coherent Light Source, SLAC National Accelerator Laboratory, Menlo Park, CA 94025, USA*

Optical images of transparent three-dimensional objects can be different from a replica of the object's cross section in the image plane, due to refraction at the surface or in the body of the object. Simulations of the object's image are thus needed for the visualization and validation of physical models, but previous image simulations for fluid dynamics showed significant differences from experiments. We report ray tracing image simulations that replicate with high fidelity brightfield microscopy images of drops with complex shapes, and images of pressure and shock waves traveling inside them. For high fidelity, the simulations must replicate the spatial and angular distribution of illumination rays, and both the experiment and the simulation must be designed for accurate optical modeling. These techniques are directly applicable to optical microscopy and expand the type and the accuracy of three-dimensional information that can be extracted from optical images.

The optical images of transparent objects are often distorted due to the refraction of light. The entire volume of the object is relevant to image formation, because rays refract at interfaces and curve through refractive index gradients. The distortion of optical images restricts the three-dimensional (3D) information that can be extracted from them. This is limiting when the objects experience rapid dynamics that preclude 3D imaging techniques such as tomography and confocal microscopy, or when the degradation of resolution with single-shot 3D imaging [1] is unacceptable.

Extracting the shape and refractive index distribution of a transparent object, from its optical image, is a difficult inverse problem. In general, it may have a unique solution only if the object has high symmetry, because the object has a higher dimensionality than the image. Instead, the 3D information hidden in the image can be exploited indirectly, by using the images to refine and validate properties calculated by other methods, such as finite-element or computational fluid dynamics (CFD) simulations. Both image-based validation and solving the inverse problem require high fidelity simulations of the direct problem, *i.e.* determining the image of an object from its 3D properties.

Ray tracing, a basic technique for understanding image formation, can be used to simulate images by tracing a large number of rays to a virtual detector [2]. While one of its best known applications is generating photorealistic images in computer graphics, some of the most sophisticated ray-tracing image simulations for real systems are related to fluid dynamics [3–5]. Fluid systems can have complex and dynamic boundaries, or nonuniform refractive index distributions. The latter are caused by the dependence of refractive index on the density, which can vary smoothly due to pressure waves, sharply due to shock waves, or jump at phase interfaces.

Ray-tracing simulations for fluid dynamics focused primarily on the visualization of the dynamics predicted by computational fluid dynamics (CFD) simulations, because simply plotting CFD-calculated object shapes and density distributions may not replicate the experimental images due to optical distortions [5]. This problem led to the development of analytical techniques for simulating experimental images [6, 7], such as plotting integrated density gradients to simulate Schlieren images [6]. Numerical ray tracing improved these early techniques. For example, tracing rays through density gradients in the object produced more realistic Schlieren images [3].

The visualization of CFD results was further improved by tracing the rays through the entire optical system, from the illumination source to the camera. This technique was applied to Schlieren and shadowgraph imaging of shocks and rarefaction waves in a gas [4], and to shadowgraph imaging of collapsing bubbles in a liquid [5]. While the experimental and simulated images were similar, there were also significant differences. For example, shadowgraph simulations generated images significantly sharper than the experimental ones [5].

The difficulties of interpreting optical images can be mitigated by using ultrafast X-ray phase contrast imaging (XPCI) [8–11]. Since X rays have a refractive index close to 1, XPCI images are less affected by refractive distortions but may have fainter image features. So far, ultrafast XPCI has been used for high contrast features such as phase boundaries and shock waves. Hydrodynamic simulations for these studies [8–11] generally
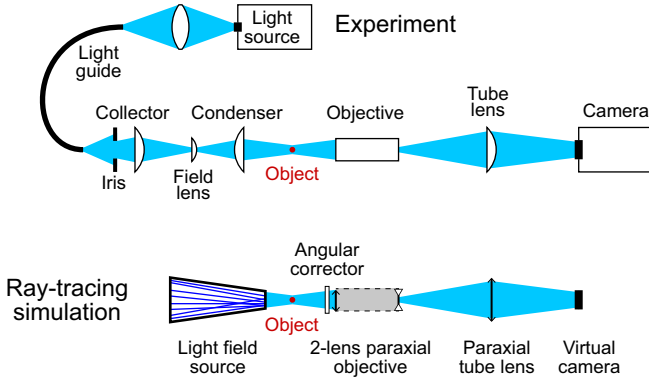
FIG. 1. The design of the ray-tracing simulation. The illumination source and optics are modeled with a virtual light field source that replicates the spatial and angular distribution of rays in the image plane, and the imaging optics are modeled with ideal lenses. The angular corrector models the angle-dependent reflective losses in the real setup.

agreed with experimental XPCI data for shock waves with amplitudes from several to hundreds of GPa, but simulations of XPCI images had low fidelity, in part due to the difficulty of calibrating the X-ray illumination [10].

Here, we report ray-tracing simulations for optical shadowgraph imaging that replicated images of spherical and non-spherical drops, in focus and out of focus, with significantly better fidelity than in previous shadowgraph simulations [5]. The simulations also replicated images of shock waves and of smooth pressure waves with amplitudes on the order of 100 MPa.

We imaged three types of water droplets in free space: spherical drops, non-spherical merging drops, and drops containing pressure waves induced by laser ablation (see the Supplemental Material for details [12]). Figure 1 illustrates the imaging setup, which is a horizontal mocroscope, and compares it with the ray-tracing model. To enable accurate simulations, the experimental setup must generate high quality images, and its components must be chosen such that they can be modeled accurately.

Since modeling more components of the optical system increases the ray tracing accuracy [4, 5], the simulation accuracy is maximized when each component is modeled. If this strategy is chosen, reflective objectives are easiest to model because they contain only two mirrors. Nevertheless, the focus field of the reflective objectives we tested was not flat enough for our experiments. Corrected refractive objectives provide sufficiently flat fields, but they have proprietary designs, so in practice they cannot be modeled as a set of discrete lenses. We chose a refractive objective that provided the required image quality and could be modeled with ideal lenses (Mitutoyo M Plan Apo 20×, NA = 0.42, infinity corrected).

The objective was paired with an f = 200 mm tube lens and a high-speed camera (Vision Research Miro M340). The optical resolution at 462 nm, with the ob-

jective aperture fully illuminated, was 0.7 μm. The illumination source was either a pulsed LED (HardSoft IL-106B, 462 nm) or a femtosecond laser (frequency-doubled Ti:sapphire laser system [13], central wavelength 405 nm). The light pulses from the source were projected into a liquid light guide to homogenize the beam (Thorlabs LLG3-6H, 3 mm diameter, 1.8 m long), and then imaged onto the sample using an f = +42.5 mm collector lens, an f = +150 mm field lens, and an f = +25 mm condenser lens. The NA of the illumination was adjusted with an iris at the collector. This setup produced a circular illuminated spot with a diameter of 2.7 mm and less than 2% intensity variation where the drops were imaged (<200 μm from the center of the spot).

The corresponding ray-tracing setup (Figure 1) modelled the entire illumination with a virtual illumination source that replicated, across the object plane, the experimental light intensity distribution and the experimental angular distribution of incoming rays. This information constitutes the 4D light field [14] of the illumination beam, thus our virtual illumination source is a light field source. The experimental light field was measured by placing a pinhole at the object location and imaging the emerging light cone on a camera. The virtual light field source was then generated by tracing rays between the images of the pinhole and of the light cone [12]. This experimentally-matched light field source was a key factor in achieving a good match between experimental and simulated images, because the drop images are highly sensitive to the light field [12].

The imaging optics were modelled with paraxial lens combinations and a virtual camera, with parameters replicating the physical ones. Since the objective had a working distance of 20 mm, longer than its 10-mm focal length, we modelled it with two paraxial lenses located at the ends of the physical objective. The lens parameters were calculated from the focal length, the working distance, and the pupil sizes of the physical objective [12]. To account for angle-dependent reflection losses in real lenses, the model includes an angular corrector placed in front of the objective. The corrector was made of a central circle surrounded by eight rings with experimentally calibrated transmission factors [12].

The model was implemented in Ansys Zemax OpticStudio (ANSYS, Inc.), and the images were simulated by tracing rays from the source to the camera. The number of rays was approximately equal to the number of photons recorded in experimental images, to match the photon shot noise. We estimated the experimental number of photons per pixel as the camera signal on a 0 to 1 scale multiplied by its electron well capacity.

Figure 2 shows a comparison of experimental and simulated images of a 46-μm diameter spherical water drop, imaged as the objective was scanned ±20 μm across the focus. The iris at the collector was fully open and the illumination rays had a maximum angle of 27°, fully filling

Experimental focusing

−20 µm (too far)   −10 µm   0 µm (focused)   +10 µm   +20 µm (too close)

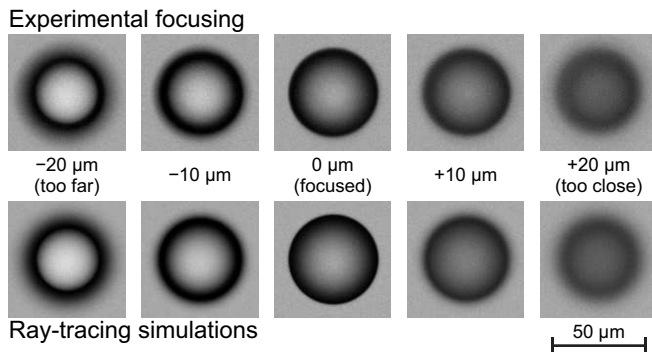Ray-tracing simulations   50 µm

FIG. 2. Reproduction of a focus scan. Experimental and simulated images of a spherical water drop are compared as the objective was focused. The simulations reproduce the intensity distribution within the drop image under all conditions.

Experiment   2D→3D→ray trace   CFD→3D→ray trace

3.5±0.5 µs   3.5±0.5 µs   3.6 µs

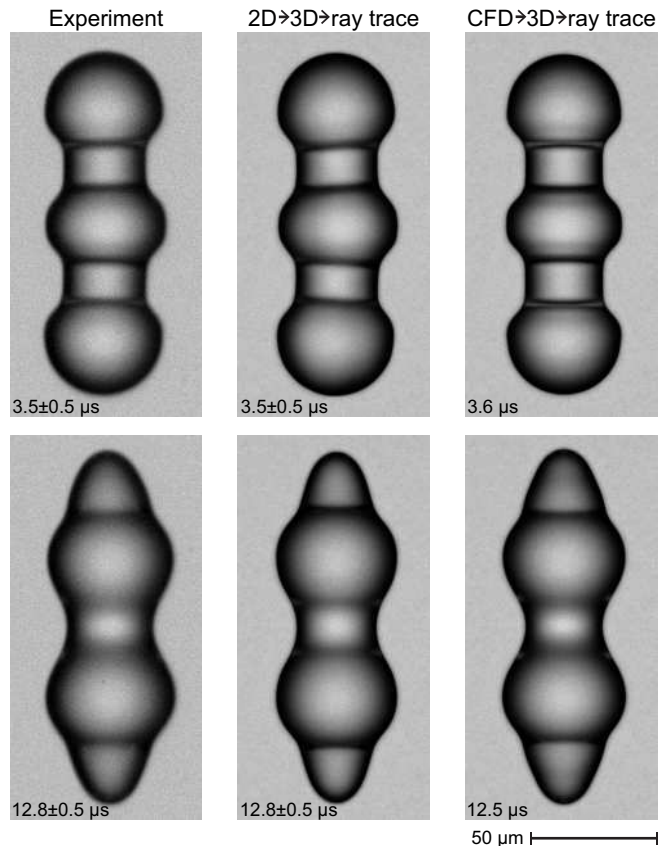12.8±0.5 µs   12.8±0.5 µs   12.5 µs

50 µm

FIG. 3. Reproduction of images of objects with complex shapes. The left column shows images of a merging drop formed by the collision of three spherical drops at time zero. The middle column shows image simulations based on a 3D drop generated by revolving the experimental 2D outline of the drop image. The right column shows image simulations of 3D drops computed using CFD.

the numerical aperture of the objective. The ray-tracing simulations reproduced accurately the experimental images over a scan distance one order of magnitude larger than the depth of focus ($\lambda/\mathrm{NA}^2 = 2.6$ µm). Additional simulations for up to ±40 µm defocusing are shown in the Supplemental Material [12]; differences from the experiment are evident only at −40 µm.

The simulated images were sharper than the experimental ones because they did not consider diffraction or the vertical motion of the drops, which blur the edges by approximately one pixel each. The simulated images were less noisy, because they did not include the electronic noise of the camera. Motion blurring, the point spread function due to diffraction, and the camera noise can be integrated in the image simulation. However, these refinements would obfuscate the performance of the ray-tracing simulations, so we did not include them.

The focus scan of a spherical drop is a sensitive test of the simulations, because slight imperfections of the model may be evident only at some focusing positions, and because it clarifies if the simulated images are unrealistically sharp [5, 7]. Focus scans for variations of the model showed that a single-lens objective model is equivalent to the two-lens model, while using a different light field or omitting the angular corrector degrades the match between simulation and experiment [12].

The ray tracing model reproduces accurately images of drops with complex shapes. Figure 3 shows images of an aspherical drop, which was generated by merging three spherical drops. The aspherical drop assumes multiple shapes as it relaxes, and Fig. 3 shows two of the observed shapes. In this case the drops cannot be modeled with a simple geometrical shape, and we used two methods to generate a three-dimensional model. The first method revolved the 2D outline of the drop from the experimental image, which generated a 3D drop. The second method calculated the 3D shape of the drop using the compressible multiphase flow solver ALPACA [15]. De-

tailed descriptions of both methods are available in the Supplemental Material [12], which also contains movies showing additional delays, for drops merging in focus and for drops merging while traveling across the focal plane.

The refraction of light by the drops in Fig. 3 leads to a pattern of light intensity across the images of the drops. These patterns are reproduced nearly identically in simulations, including subtly brighter or darker regions. Overall, the simulated images replicated the experimental ones with higher fidelity than in previous studies [5]. Slight differences between experiment and simulations exist because the simulated drops did not replicate perfectly the shape of the experimental drops, which were not precisely axisymmetric.

A stringent test of the ray-tracing simulations is replicating images of objects with smooth spatial variations in their refractive index. In this case, the image cannot be understood as a mapping of the 3D object space onto the 2D image space, because the object does not have sharp identifiable features. As a test of this case, we simulated

images of water drops ablated by an X-ray laser pulse. The drops were imaged optically after they were exposed to a femtosecond X-ray laser pulse passing approximately through the center of the drop. The X rays heated isochorically a thin filament of water to high temperatures and pressures, which launched a cylindrical shock wave. The shock reflected at the surface of the drop, generating a converging negative pressure wave [16].

The experimental ablation images were recorded at the CXI instrument of the LCLS X-ray laser facility [13, 17], using 43 μm diameter water drops. The imaging system was identical to the one used for the spherical and the merging drops, except for (i) using laser pulses for illumination, and (ii) reducing the maximum illumination angle to approximately 23° to enhance the contrast of waves. The X-ray pulse energy was below the threshold for generating secondary cavitation (spallation) in the drops [16], which allowed us to observe the negative pressure wave converging to a focus and then expanding.

The simulated images used virtual drops with properties calculated using ALPACA [15]. Previous results showed that high-resolution numerical simulations can reproduce the X-ray ablation dynamics [18]. We adjusted the initial conditions of the CFD model to replicate the experimental motion of the drop surface during shock reflection [12, 16, 19]. We also optimized the NASG equation of state [20] used in the CFD simulations to match the adiabatic and shock compression paths predicted by the IAPWS-95 equation of state [12, 21]. The results of the CFD simulations provided the 3D shape of the drops, and their internal pressure and density distributions. The refractive index distribution was calculated from the density distribution, the temperature of the drop, and a light wavelength of 400 nm [22].

Figure 4 shows experimental and simulated images of an expanding shock wave with an CFD-calculated amplitude of 70 MPa, and of a converging negative pressure wave with an amplitude of −110 MPa [12]. The simulations replicate the width and intensity of the shock better than it was previously achieved with either brightfield or Schlieren imaging [4]. The image of the negative pressure wave, which to our knowledge is the first replication of a smooth pressure wave in brightfield images, matched the experimental aspect ratio and the pattern of dark and bright modulations. Comparisons at additional time delays are available as movies in the Supplemental Material [12], for the experiment shown in Fig. 4 and for another one with a lower energy X-ray pulse, which generated visible pressure waves without producing ablation holes. The movies show that our simulations replicate a counterintuitive optical effect—the shocks become more visible as they propagate, despite becoming weaker.

Due to experimental and CFD limitations, the overall match of images for ablated drops is worse than for the merging drops. For the ablation simulations, we had to use a surrogate light field that did not reproduce a bright
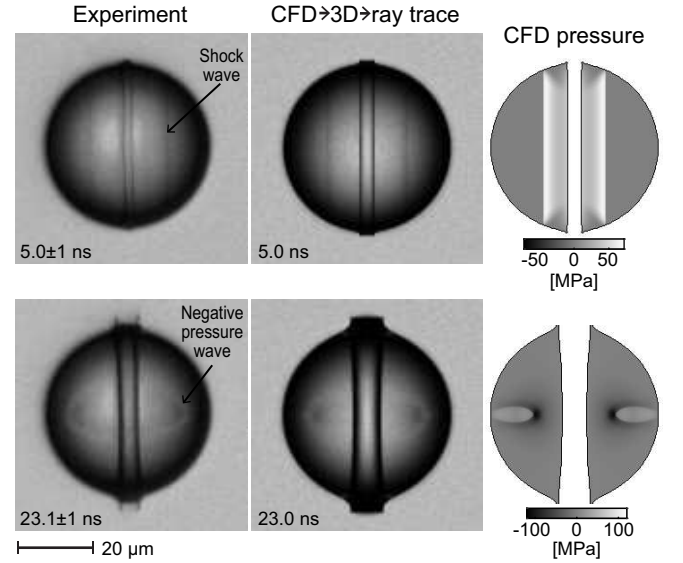

FIG. 4. Reproduction of images of laser-ablated drops with internal pressure waves. The image simulations replicate the width and the intensity of shock waves and of negative pressure waves, and are qualitatively different from the corresponding 2D pressure distributions in the image plane. The central vertical feature is an ablation hole, which has a different size in simulations because it is approximated in the CFD model.

spot in the experimental images. Additionally, the image of the negative pressure wave was sensitive to misalignments between the drop and the X-ray pulse [12], and might be more sensitive to the accuracy of the CFD model than the image of the shock. The images of the ablation hole differ because the CFD simulation starts with a formed ablation hole, while in the experiment the core forms gradually. Even with these limitations, the simulated images had a higher degree of fidelity than in XPCI studies [10].

The high fidelity of our image simulations enabled us to refine and validate the CFD models, and to detect experimental features that were not interpretable from optical images, such as an 1° rotation of merging drops along the imaging direction [12]. Another benefit of the high fidelity is the ability to constrain density and pressure measurements [12]. Simulated images of the shock wave shown in Fig. 4 had a worse match with the experiment if their amplitude was different by ±10 MPa. We also estimated the potential sensitivity of measuring pressures with image simulations by varying the amplitude of the pressure wave from the weak ablation experiment. A density change of 4 kg/m^3, corresponding to a pressure change of 8 MPa, could be detected between simulated images. This density change corresponds to changes in the projected mass density below 10^{-5} kg/m^2, orders of magnitude smaller than the mass density differences observed in XPCI [10].

Here, we found that high fidelity ray-tracing image simulations required two new techniques: using a light field source, and testing the fidelity of the simulations via focus scans. Starting with these techniques, the experiment, the image simulation, and auxiliary models can be refined effectively for high image fidelity. Here, the agreement between experiments and simulations validated both the ray-tracing and the CFD models. With high fidelity image simulations, it also becomes possible to develop iterative algorithms for measuring 3D properties such as shape and density directly from 2D images. Since our findings are applicable to microscopy, they could enable higher accuracy in other fields, such as microfluidics or biology.

* Email: claudiu.stan@rutgers.edu

[1] M. Levoy, R. Ng, A. Adams, M. Footer, and M. Horowitz, Light field microscopy, ACM T. Graphic. **25**, 924 (2006).

[2] A. S. Glassner, *An introduction to ray tracing* (Morgan Kaufmann, 1989).

[3] C. Brownlee, V. Pegoraro, S. Shankar, P. S. McCormick, and C. D. Hansen, Physically-based interactive flow visualization based on schlieren and interferometry experimental techniques, IEEE T. Vis. Comput. Gr. **17**, 1574 (2011).

[4] E. Luthman, N. Cymbalist, D. Lang, G. Candler, and P. Dimotakis, Simulating schlieren and shadowgraph images from les data, Exp. Fluids **60**, 134 (2019).

[5] M. Koch, J. M. Rosselló, C. Lechner, W. Lauterborn, J. Eisener, and R. Mettin, Theory-assisted optical ray tracing to extract cavitation-bubble shapes from experiment, Exp. Fluids **62**, 60 (2021).

[6] L. A. Yates, Images constructed from computed flow-fields, AIAA J. **31**, 1877 (1993).

[7] G. S. Settles and M. J. Hargather, A review of recent developments in schlieren and shadowgraph techniques, Meas. Sci. Technol. **28**, 042001 (2017).

[8] A. Schropp, R. Hoppe, V. Meier, J. Patommel, F. Seiboth, Y. Ping, D. G. Hicks, M. A. Beckwith, G. W. Collins, A. Higginbotham, J. S. Wark, H. J. Lee, B. Nagler, E. C. Galtier, B. Arnold, U. Zastrau, J. B. Hastings, and C. G. Schroer, Imaging shock waves in diamond with both high temporal and spatial resolution at an xfel, Sci. Rep. **5**, 11089 (2015).

[9] M. Vassholz, H. P. Hoeppe, J. Hagemann, J. M. Rosselló, M. Osterhoff, R. Mettin, T. Kurz, A. Schropp, F. Seiboth, C. G. Schroer, M. Scholz, J. Möller, J. Hallmann, U. Boesenberg, C. Kim, A. Zozulya, W. Lu, R. Shayduk, R. Schaffer, A. Madsen, and T. Salditt, Pump-probe x-ray holographic imaging of laser-induced cavitation bubbles with femtosecond fel pulses, Nat. Comm. **12**, 3468 (2021).

[10] D. S. Hodge, N. F. T. Leong, S. Pandolfi, K. Kurzer-Ogul, D. S. Montgomery, H. Aluie, C. Bolme, T. Carver, E. Cunningham, C. B. Curry, M. Dayton, F. J. Decker, E. Galtier, P. Hart, D. Khaghani, H. J. Lee, K. A. Li, Y. W. Liu, K. Ramos, J. S. C. Shang, S. Vetter, B. Nagler, R. L. Sandberg, and A. E. Gleason, Multi-frame, ultrafast, x-ray microscope for imaging shockwave dynamics, Opt. Express **30**, 38405 (2022).

[11] S. Makarov, S. Dyachkov, T. Pikuz, K. Katagiri, H. Nakamura, V. Zhakhovsky, N. Inogamov, V. Khokhlov, A. Martynenko, B. Albertazzi, G. Rigon, P. Mabey, N. J. Hartley, Y. Inubushi, K. Miyanishi, K. Sueda, T. Togashi, M. Yabashi, T. Yabuuchi, T. Okuchi, R. Kodama, S. Pikuz, M. Koenig, and N. Ozaki, Direct imaging of shock wave splitting in diamond at mbar pressure, Matter Radiat. Extremes **8**, 066601 (2023).

[12] See Supplemental Material [url] for supplementary videos and for a text file with further details of experiments and models, which includes Refs. [23-27].

[13] M. Liang, G. J. Williams, M. Messerschmidt, M. M. Seibert, P. A. Montanez, M. Hayes, D. Milathianaki, A. Aquila, M. S. Hunter, J. E. Koglin, D. W. Schafer, S. Guillet, A. Busse, R. Bergan, W. Olson, K. Fox, N. Stewart, R. Curtis, A. A. Miahnahri, and S. Boutet, The coherent x-ray imaging instrument at the linac coherent light source, J. Synchrotron Radiat. **22**, 514 (2015).

[14] M. Levoy and P. Hanrahan, Light field rendering, in *Seminal Graphics Papers: Pushing the Boundaries*, Vol. 2, edited by M. C. Whitton (ACM, USA, 2023) pp. 441–452.

[15] N. A. Adams, S. Adami, V. Bogdanov, A. Buhendwa, A. Bußmann, N. Fleischmann, N. Hoppe, N. Hosseini, J. Kaiser, A. Lunkov, T. Paula, F. Spaeth, A. Siguenza Torres, P. Wauligmann, J. Winter, and T. Gymnich, *ALPACA - Adaptive Level-set PArallel Code Alpaca*, Technical University of Munich, Garching, Germany (2022).

[16] C. A. Stan, P. R. Willmott, H. A. Stone, J. E. Koglin, M. Liang, A. L. Aquila, J. S. Robinson, K. L. Gumerlock, G. Blaj, R. G. Sierra, S. Boutet, S. A. H. Guillet, R. H. Curtis, S. L. Vetter, H. Loos, J. L. Turner, and F. J. Decker, Negative pressures and spallation in water drops subjected to nanosecond shock waves, J. Phys. Chem. Lett. **7**, 2055 (2016).

[17] P. Emma, R. Akre, J. Arthur, R. Bionta, C. Bostedt, J. Bozek, A. Brachmann, P. Bucksbaum, R. Coffee, F. J. Decker, Y. Ding, D. Dowell, S. Edstrom,

A. Fisher, J. Frisch, S. Gilevich, J. Hastings, G. Hays, P. Hering, Z. Huang, R. Iverson, H. Loos, M. Messerschmidt, A. Miahnahri, S. Moeller, H. D. Nuhn, G. Pile, D. Ratner, J. Rzepiela, D. Schultz, T. Smith, P. Stefan, H. Tompkins, J. Turner, J. Welch, W. White, J. Wu, G. Yocky, and J. Galayda, First lasing and operation of an angstrom-wavelength free-electron laser, Nat. Photon. **4**, 641 (2010).

[18] T. Paula, S. Adami, and N. A. Adams, Analysis of the early stages of liquid-water-drop explosion by numerical simulation, Phys. Rev. Fluids **4**, 044003 (2019).

[19] C. A. Stan, K. Motomura, G. Blaj, Y. Kumagai, Y. W. Li, D. You, T. Ono, A. Kalita, T. Togashi, S. Owada, K. Tono, M. Yabashi, T. Katayama, and K. Ueda, The magnitude and waveform of shock waves induced by x-ray lasers in water, Appl. Sci.-Basel **10**, 1497 (2020).

[20] O. Le Métayer and R. Saurel, The noble-abel stiffened-gas equation of state, Phys. Fluids **28**, 046102 (2016).

[21] W. Wagner and A. Pruß, The iapws formulation 1995 for the thermodynamic properties of ordinary water substance for general and scientific use, J. Phys. Chem. Ref. Data **31**, 387 (2002).

[22] A. H. Harvey, J. S. Gallagher, and J. Sengers, Revised formulation for the refractive index of water and steam as a function of wavelength, temperature and density, J. Phys. Chem. Ref. Data **27**, 761 (1998).

[23] A. Kalita, M. Mrozek-McCourt, T. F. Kaldawi, P. R. Willmott, N. D. Loh, S. Marte, R. G. Sierra, H. Laksmono, J. E. Koglin, M. J. Hayes, R. H. Paul, S. A. H. Guillet, A. L. Aquila, M. N. Liang, S. Boutet, and C. A. Stan, Microstructure and crystal order during freezing of supercooled water drops, Nature **620**, 557 (2023).

[24] C. A. Stan, A. Kalita, and M. Mrozek-McCourt, *Modeling of supercooling, solidification, and freezing stages of water drops*, Zenodo (2023).

[25] T. Paula, S. Adami, and N. A. Adams, A robust high-resolution discrete-equations method for compressible multi-phase flow with accurate interface capturing, J. Comput. Phys. **491**, 112371 (2023).

[26] N. Vargaftik, B. N. Volkov, and L. Voljak, International tables of the surface tension of water, J. Phys. Chem. Ref. Data **12**, 817 (1983).

[27] C. A. Stan, A. Kalita, S. Marte, T. F. Kaldawi, P. R. Willmott, and S. Boutet, Rocket drops: The self-propulsion of supercooled freezing drops, Phys. Rev. Fluids **8**, L021601 (2023).